Preparation and Electrochemical Properties of Gadolinium Oxide –doped Carbon Aerogels/Sulfur Composites

Anqiao Zheng[1], Rui Liang[2], Han Wu[1], Guodong Jiang[1,3], Mingxia Fan[1,3], Jian Xiong[1,3], Songdong Yuan[1,3,*]

[1] Hubei Collaborative Innovation Center for High-efficiency Utilization of Solar Energy, Hubei University of Technology, Wuhan 430068, China
[2] Sunwoda Electronic Co.,Ltd, Shenzhen 518108, China
[3] The Synergistic Innovation Center of Catalysis Materials of Hubei Province, Wuhan 430068, China
[*]E-mail: 171245675@qq.com

A carbon aerogel (CA) was successfully synthesized by a sol-gel method combined with freeze-drying, followed by solution permeation impregnation and high-temperature carbonization to obtain a gadolinium oxide (Gd_2O_3)–doped CA composite ($CA@Gd_2O_3$). Then, $CA@Gd_2O_3$ was incorporated with sulfur by the melt-diffusion method to obtain $CA@Gd_2O_3@S$ composites, which exhibited a superior electrochemical performance. The initial discharge specific capacity of the composite reached 1168.4 mAh/g at 0.1 C and maintained a reversible specific capacity of 814.4 mAh/g after 100 cycles. The outstanding electrochemical properties were mainly attributed to the strong polar adsorption of polysulfides by the abundant O^{2-} ions on the surface of Gd_2O_3, which inhibited the shuttle effect of polysulfides. Moreover, the CA doped with Gd_2O_3 maintained a high specific surface area and large pore capacity to alleviate the poor electrical conductivity and volume expansion effect of sulfur cathode materials.

1. INTRODUCTION

With the emphasis on environmental protection and the strong support for electric vehicles in many countries, the development of electric vehicles has become increasingly rapid. The lithium-ion battery was officially commercialized in 1991, but it still cannot fully meet energy-storage needs despite decades of development. The current mainstream lithium-ion battery cathode materials, such as ternary materials [1], lithium iron phosphate [2-3], and lithium cobaltate [4], are gradually approaching their theoretical specific capacity, but their highest energy density is only approximately 250 Wh/kg, which will exert low endurance when used as the energy source for large devices such as electric vehicles.

Therefore, the search and development of a new generation of low-cost secondary lithium battery cathode materials with high energy density, long cycle life, and environmental friendliness has become a current research hot spot [5-7].

Sulfur has the advantages of high theoretical specific capacity (1675 mAh/g) and energy density (2600 Wh/kg) when used as the cathode material for lithium-ion batteries, and it is widely available, abundant, and inexpensive [8]. However, obstacles that prevent its commercialization include the shuttle effect of polysulfides, as well as poor electrical conductivity and volume expansion effects [9-10]. To solve these problems, numerous researchers have made painstaking efforts, including combining sulfur with carbon materials such as porous carbon [11], carbon nanotubes [12], graphene [13], carbon nanofibers [14], and hollow carbon spheres [15]. The rich pore structure of carbon materials allows for greater loading of sulfur, improves the electrical conductivity of the material, and alleviates the volume expansion effect. In addition, the physical domain–limiting effect of carbon materials can also suppress the shuttle effect of polysulfide to a certain extent. However, the physical adsorption of carbon materials is weak and cannot fully meet the demand [16]. Therefore, carbon materials are mostly used for lithium-sulfur battery cathode materials after compounding with heteroatoms or metal compounds [17].

Shu et al. [18] prepared an in-situ high-content N-doped carbon aerogel (CA) for sulfur loading and found that composites with a high nitrogen content could achieve a strong adsorption of lithium polysulfides with excellent electrochemical properties due to the inherent N active site of the CA. Qi et al. [19] synthesized sulfur-impregnated SnO_2/carbon aerogel (SnO_2/CA@S) core-shell microspheres as a polysulfide absorbent for lithium-sulfur batteries. The core of the CA microspheres was designed to accommodate an increasing volume, and the tin-oxide shell acted as an efficient polysulfide trap. Compared with an unloaded SnO_2 composite, SnO_2/CA@S showed an enhanced reversible capacity (949 mAh/g at 0.1 C), with a capacity retention of 76.9% after 80 cycles. However, the initial specific capacity of the material was only about half of the theoretical specific capacity, which may be due to the inherently poor conductivity and the shuttle effect of the polysulfides.

Rare earth metal compounds refer to oxides composed of 15 lanthanides, as well as scandium (Sc) and yttrium (Y), with similar properties to lanthanides. Moreover, rare earth elements have important applications in many materials fields and are also known as "21st century gold" [20]. When they are used in lithium-ion batteries, polar adsorption can be used to improve the electrochemical cycle stability of lithium-ion batteries [21].

Herein, a kind of CA with high specific surface area and rich void structure was prepared by a sol-gel method and used to improve the electrical conductivity of sulfur. In addition, a solution infiltration method and high temperature pyrolysis were used to dope the CA with gadolinium oxide (Gd_2O_3), relying on the polar adsorption effect of rare earth metal Gd_2O_3 to suppress the shuttle effect of polysulfide. The cycle stability and rate performance of sulfur were improved, and the optimal addition of Gd_2O_3 was evaluated.

2. EXPERIMENTAL

2.1. Materials

Resorcinol, Na_2CO_3, formaldehyde, sulfur, and anhydrous ethanol were of analytical grade and purchased from Sinopharm Chemical Reagent Co., Ltd. (Shanghai, China). $Gd(NO_3)_3 \cdot 6H_2O$ was of analytical grade and purchased from Aladdin Biochemical Technology Co., Ltd. (Shanghai, China). These reagents were used as received.

2.2. Preparation of carbon aerogels (CA)

First, 0.05 mol of resorcinol (R) was dissolved in 30 mL of deionized water before adding 0.1 mmol of sodium carbonate (C) as a catalyst; this was then dissolved and kept magnetically stirred for 0.5 h, before adding 0.1 mol of formaldehyde (F) and magnetically stirring for 1 h. The solution was mixed well, placed in a water bath at 85°C, and maintained at a constant temperature for 3 days. After the reaction, the solution was cooled to room temperature and freeze-dried for 24 h. Finally, the resulting material was heated to 850°C under Ar atmosphere at a heating rate of 5°C/min and held for 2 h to produce a CA. The specific material ratios were R: C = 500: 1, R: F = 1: 2, and the overall concentration of the reaction system was adjusted to approximately 20% by adding an appropriate amount of deionized water.

2.3. Synthesis of $CA@Gd_2O_3$

Then, 0.4 g of the prepared CA was added to a beaker containing 30 mL of anhydrous ethanol and sonicated for 10 min, followed by the addition of different masses of gadolinium nitrate hexahydrate and continued sonication for 20 min to dissolve and adhere the gadolinium nitrate to the pore structure of the CA. The beaker was then heated in a water bath at 70°C for 1 h to allow the ethanol to evaporate and separate. The resulting material was then placed in a tube furnace and heated to 720°C under Ar atmosphere at a heating rate of 5°C/min and held for 1 h to decompose the gadolinium nitrate to obtain the Gd_2O_3-doped CA. In this experimental scheme, the doping amount of Gd_2O_3 was mainly controlled by the addition of gadolinium nitrate hexahydrate, which was added according to Gd: C = 1: 400, 1: 200, 1: 100 (ratio of molar). A blank control group without gadolinium nitrate hexahydrate was made, and the four materials were denoted as CA and $CA@Gd_2O_3$-n (n = 1, 2, 3).

2.4. Synthesis of $CA@Gd_2O_3@S$

In lithium-sulfur battery cathode materials, the loading process of active substance sulfur is generally carried out by the melt-diffusion method, which is also the case in this experiment. The prepared $CA@Gd_2O_3$ was mixed with sulfur at a mass ratio of 3:7 and ground thoroughly in an agate mortar to mix well. After that, it was placed in a corundum boat and heated to 155°C in a tube furnace under an Ar atmosphere at a rate of 5°C/min for 12 h. Heating was then continued at a rate of 5°C/min

to 300°C for 1 h to remove as much sulfur as possible adhering to the surface of the composite. After cooling to room temperature, the $CA@Gd_2O_3@S$ composite cathode material was obtained by fully grinding with an agate mortar. The composites corresponding to CA and $CA@Gd_2O_3$-n loaded with sulfur were denoted as CA@S and $CA@Gd_2O_3@S$-n (n = 1, 2, 3), respectively.

2.5. Characterizations

X-ray powder diffraction (PANalytical Empyrean) was conducted to collect crystalline phase data of the samples. The test conditions were as follows: Cu Kα (λ=0.15405 nm), tube voltage 45 kV, tube current 40 mA, and scan rate 5°/min. The morphologies of the samples were characterized by field emission scanning electron microscopy (SEM, ZEISS MERLIN Compact) and high-resolution transmission electron microscopy (TEM, FEI TF-20). The elements were identified by energy dispersive spectroscopy (EDS). X-ray photoelectron spectroscopy (XPS, Thermo Fisher K-Alpha+) measurements were carried out to determine the elemental valence and structure of the samples.

2.6. Electrochemical measurements

To investigate the electrochemical performance of these samples, the active materials (CA@S, $CA@Gd_2O_3@S$-1, $CA@Gd_2O_3@S$-2, and $CA@Gd_2O_3@S$-3) mixed with conductive carbon black and polyvinylidene fluoride (PVDF) at a mass ratio of 7:2:1 was dispersed in N-methyl pyrrolidone and stirred for 8 h and then coated on the aluminum collector, followed by drying at 80°C overnight. Using Al foil loaded with the active material as the working electrode, a lithium metal electrode as a reference and counter electrode, 1 M LiTFSI in 1,3-dioxolane/ethylene glycol dimethyl ether (V: V= 1: 1) as the electrolyte (1 wt% lithium nitrate was added to the electrolyte) and microporous polypropylene film (Celgard 2400) as a separator were assembled into a half-cell (CR 2032) in a glove box filled with Ar (Mikrouna, China, $[O_2]$ < 0.1 ppm, $[H_2O]$ < 0.1 ppm). A charge–discharge test was conducted on a CT2001a battery tester (LAND Electronic Co.) at room temperature, and the corresponding potential window was set in the range of 1.7–2.8 V. Cyclic voltammogram (CV) results for the first 3 cycles were obtained on the electrochemical workstation (Donghua, China) with a sweep rate of 0.1 mV/s. AC electrochemical impedance spectroscopy (EIS) was performed at an electrochemical workstation between 10 mHz and 100 kHz with an amplitude of 5 mV.

3. RESULTS AND DISCUSSION

Figure 1 shows the XRD of CA, $CA@Gd_2O_3$-2, and $CA@Gd_2O_3@S$-2, from which the following information can be obtained. For the pure CA, two broad peaks appeared near 2θ = 22° and 44°, corresponding to the (002) and (100) crystallographic planes of graphite, respectively, indicating that the pure CA had an amorphous structure [22-23]. After doping with Gd_2O_3, the characteristic diffraction peaks at 2θ = 28.5°, 47.5° and 56.4° for the $CA@Gd_2O_3$-2 composite corresponded to the (222), (440),

and (622) crystal planes of Gd_2O_3 (JCPDS 43-1014) [24], showing that Gd_2O_3 was successfully synthesized.
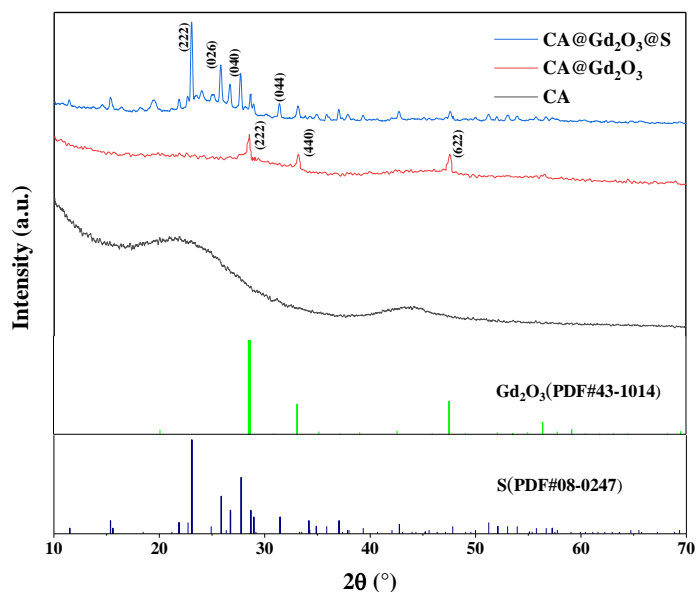

Figure 1. The XRD patterns of CA, CA@Gd_2O_3-2, and CA@Gd_2O_3@S-2 composites.

The characteristic diffraction peaks at $2\theta = 23.1°$ and $27.8°$ corresponded to the (222) and (040) crystallographic planes of sulfur, respectively, disclosing that the sulfur crystallography was rhombohedral [25], and the intensity of sulfur diffraction peaks was weak due to the uniform distribution of sulfur in the pore structure of the composite.

To confirm the actual active substance sulfur loading of the composite electrode materials, thermogravimetric analysis of CA@S and CA@Gd_2O_3@S-n (n = 1, 2, 3) composites under Ar gas conditions were performed, as shown in Figure 2. From the results of the thermogravimetric variation curves, it can be concluded that the actual sulfur loadings were 60.8%, 48.8%, 49.1% and 58.7%. The trend curve of sulfur sublimation weight-loss was divided into two main stages: the first stage is the sulfur stored in the surface void structure of the carbon material between 180°C and 300°C, and the second stage is the sulfur stored in the deep pore structure of the carbon material above 300°C. From the general trend, it can be seen that the CA doped with Gd_2O_3 loads less sulfur compared with the pure CA, which is due to the fact that the Gd_2O_3 doping causes some of the pore structures of the CA to be blocked, resulting in a reduced loading of sulfur. However, the reduced loading has less effect on the specific capacity of the composite material, and Gd_2O_3 can further inhibit the shuttle effect of polysulfide through polar adsorption, which is beneficial for improving the cycle stability of the composites.
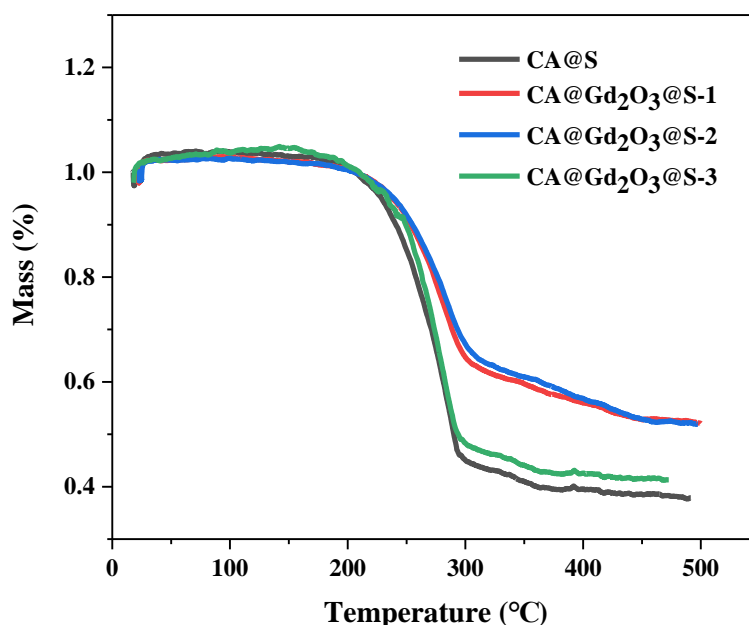
Figure 2. TGA curves of CA@S and CA@Gd$_2$O$_3$@S-n (n = 1, 2, 3) composites.

As sulfur carriers, CAs and their specific surface area and pore structure have a great impact on sulfur loading. The isothermal adsorption and desorption curves of CA and CA@Gd$_2$O$_3$-2 composites for nitrogen were investigated, as shown in Fig. 3. Figure 3(a) shows N$_2$ adsorption-desorption isotherms of CA and CA@Gd$_2$O$_3$-2. According to the International Union of Pure and Applied Chemistry classification, the two carbon materials have obvious H4-type hysteresis loops in the range of P / P$_0$ = 0.5-0.9, indicating that they have a mesoporous structure [26-27]. Based on the Brunauer–Emmett–Teller (BET) theory, the specific surface area and pore volume of the CA are 722.27 m^2/g and 1.239 cm^3/g, respectively, and the corresponding values for CA@Gd$_2$O$_3$-2 are 577.94 m^2/g and 1.077 cm^3/g. These result indicate that Gd$_2$O$_3$ doping has little effect on the overall pore structure of the CAs, and CA@Gd$_2$O$_3$-2 still has a very high specific surface area. Therefore, we can conclude that the doping of Gd$_2$O$_3$ has little effect on the specific surface area of the material and provides more polar adsorption sites for the adsorption of polysulfides. In addition, the larger pore volume can further alleviate the volume expansion effect of active substances during charging and discharging [28]. Although the overall specific surface area of the Gd$_2$O$_3$-doped composites decreases, the doped Gd$_2$O$_3$ can effectively adsorb polysulfides and reduce the loss of sulfur. Fig. 3(b) shows the pore size distribution of the two materials. After calculation, it is found that the pore diameters of CA and CA@Gd$_2$O$_3$-2 are mainly distributed near 13.4 nm, indicating that Gd$_2$O$_3$ doping has no significant effect on the pore size of carbon materials.
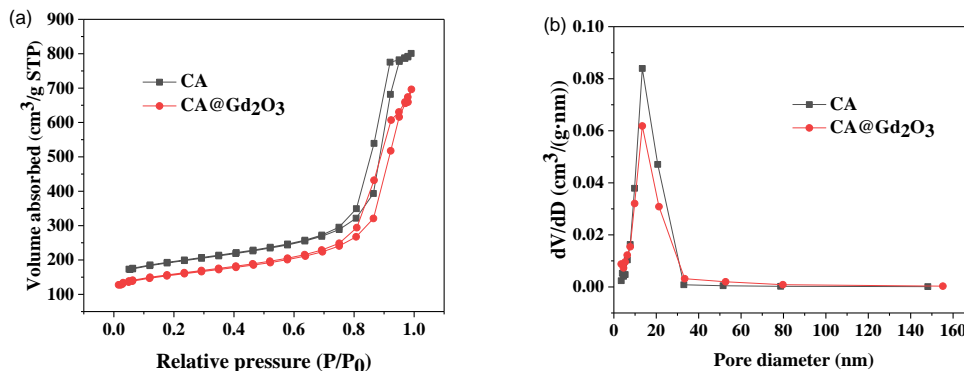
Figure 3. (a) N_2 adsorption-desorption isotherms of CA and CA@Gd_2O_3-2; (b) BJH pore size distributions of CA and CA@Gd_2O_3-2.

To investigate the morphology of CAs and the effect of Gd_2O_3 doping on their structures, SEM was conducted on the three composites. As shown in Figure 4(a), the morphology of the pure CA reveals that the CA prepared by the sol-gel method has a mutually cross-linked nanosphere structure, as well as a rich pore structure. This is conducive to the storage of active material sulfur and the rapid transport of lithium ions, and the porous material provides a favorable structural basis for improving the electrochemical performance of lithium-sulfur batteries. Figure 4(b, c) shows SEM images of the CA@Gd_2O_3-2 and CA@Gd_2O_3@S-2. It can be seen that Gd_2O_3 doping had no effect on the morphology of the CA, and it remained rich in pores and cross-linked structure. This also indicates that Gd_2O_3 enters the pore structure of the CA. Moreover, it can also be found that the morphology of CA@Gd_2O_3@S-2 was basically unchanged compared with that before loading, with no large lumps or obvious agglomerates on the surface. This demonstrated that the active substance sulfur has been uniformly dispersed in the pore structure of the CA and suggests that Gd_2O_3 can better exploit the physically limiting effects of CAs and effectively improve the utilization of active substances. Figure 4(d–h) shows the EDS element distribution of the CA@Gd_2O_3@S-2 composites, from which it can be seen that the gadolinium element and sulfur element were more uniformly distributed in the composites without any agglomeration phenomenon. This also demonstrated that the Gd_2O_3 and sulfur are uniformly dispersed in the pore structure of the CA.

TEM was also performed on the CA@Gd_2O_3 composites to further verify their specific morphology and microstructure. Figure 5(a, b) shows TEM images of the CA@Gd_2O_3-2 composite at low magnification. As shown in Figure 5(a), the part that occupies most of the image area and is lightly shaded is the carbon nanospheres of the CA, and the darker color is the Gd_2O_3 particles. It can be seen that the Gd_2O_3 nanoparticles, with a diameter of approximately 5 nm, are more uniformly distributed in the CA.
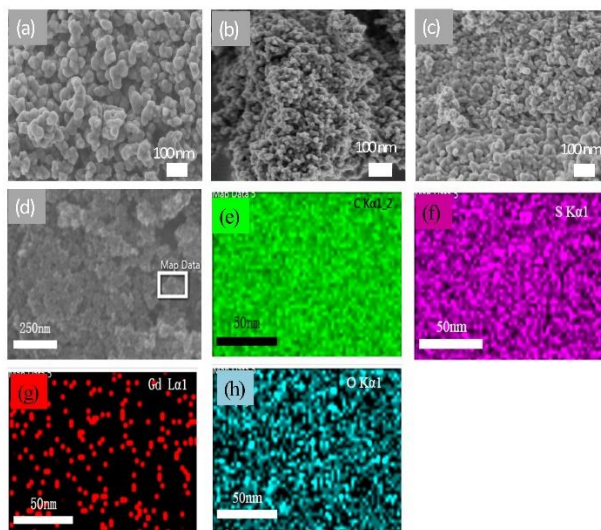
Figure 4. (a–c) SEM images of CA, CA@Gd$_2$O$_3$-2, and CA@Gd$_2$O$_3$@S-2; (d–h) EDS element distribution maps of CA@Gd$_2$O$_3$@S-2 (C, S, Gd, and O).
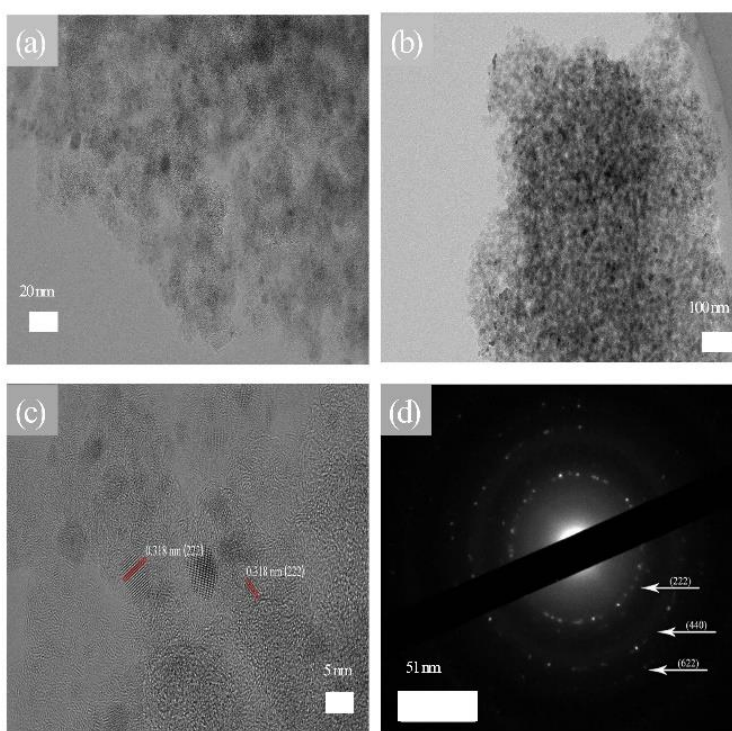
Figure 5. (a and b) TEM images of CA@Gd$_2$O$_3$-2, (c) HRTEM images of CA@Gd$_2$O$_3$-2, (d) SAED images of CA@Gd$_2$O$_3$-2.

Figure 5(c) shows a high-resolution TEM image of the CA@Gd$_2$O$_3$-2 composite, presenting a distinct lattice pattern with a spacing of 0.318 nm, which agrees well with the (222) crystalline surface of Gd$_2$O$_3$. The selected area electron diffraction (SAED) images of CA@Gd$_2$O$_3$-2 in Fig. 5(d) show that the composite exhibits a typical polycrystalline diffusion ring pattern, where the diffusion ring can

correspond to the (222), (440), and (622) lattice, respectively, corresponding to the lattice of Gd_2O_3. The lattice pattern of HRTEM and the polycrystalline diffraction ring results of SAED both confirm the successful synthesis of Gd_2O_3 and its uniform distribution in the composite.

To investigate the elemental composition of the composite surface and its chemical state, XPS characterization was performed for CA and CA@Gd_2O_3-2, and the results are shown in Figure 6. Figure 6(a) shows the XPS full spectra of CA and CA@Gd_2O_3-2, from which it can be seen that both CA and CA@Gd_2O_3-2 have C 1s and O 1s peaks [29], and CA@Gd_2O_3-2 also shows a Gd 4d peak [30], indicating that CA@Gd_2O_3-2 contains gadolinium elements. To further investigate the chemical state of Gd in the composites, this section also analyzes the XPS high-resolution spectra of CA@Gd_2O_3-2 with peak splitting, as shown in Figure 6(b–d) for the XPS high-resolution C 1s, O 1s, and Gd 4d energy spectra, respectively. The four fitted peaks at 284.6, 285.4, 286.4, and 289.1 eV in the C 1s spectrum correspond to C-C, C-O, C=O, and O-C=O bonds, respectively. The fitted peaks at 531.5, 532.4, and 533.4 eV in the O 1s spectrum correspond to the Gd–O, C–O, and C–O–C bonds, respectively. The fitted peak at 143.6 eV in the Gd 4d spectrum also corresponds to the Gd–O bond [31]. From the XPS characterization results, it can be concluded that Gd_2O_3 was successfully synthesized in CA matrix materials. Gd_2O_3 can be used as polar sites to adsorb polysulfides to suppress the shuttle effect of polysulfides and improve the cycle stability of composite cathode materials for lithium-sulfur batteries.
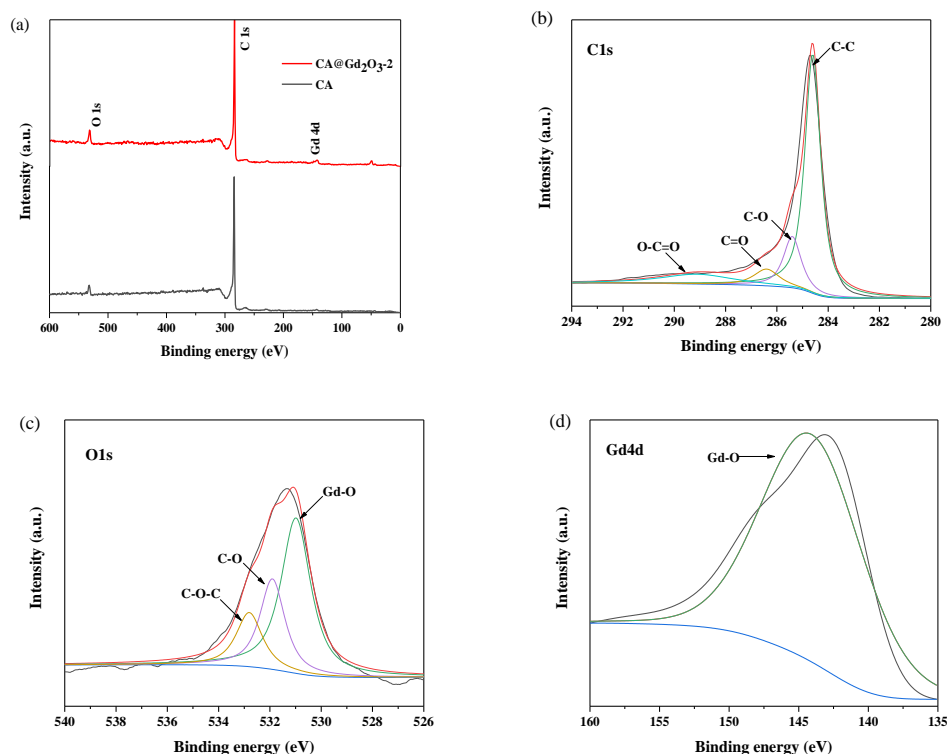

Figure 6. (a) Survey XPS spectrum of CA and CA@Gd_2O_3-2, and high resolution XPS spectra of (b) C 1s, (c) O 1s, and (d) Gd 4d for CA@Gd_2O_3-2.

The constant-current charge/discharge cycles of CA@S and CA@Gd_2O_3@S-n composite cathode materials were mainly tested at different rates in this section, and the cycle stability were

analyzed based on the results. Figure 7(a) shows the first cycle charge and discharge curves of the CA@S and CA@Gd$_2$O$_3$@S-n at 0.1 C. It can be noticed that the four samples discharge near 2.25 V and 2.05 V. The formation of these two discharge plateaus can be attributed to the two-step reaction of sulfur in the discharge process. The sulfur first forms long-chain polysulfides, and the long-chain polysulfides then further react and convert to short-chain polysulfides and insoluble lithium sulfide. There is an obvious charging plateau at 2.30 V, which is mainly due to the step-by-step oxidation of short-chain polysulfides and insoluble lithium sulfide toward long-chain polysulfides and sulfur. To analyze the cycle stability of the material, long-cycle charge–discharge tests were carried out. Figure 7(b) shows the charge–discharge cycle curves of the CA@S and CA@Gd$_2$O$_3$@S-n composite cathode materials at a low rate of 0.1 C. The initial discharge specific capacities of CA@S, CA@Gd$_2$O$_3$@S-1, CA@Gd$_2$O$_3$@S-2, and CA@Gd$_2$O$_3$@S-3 were 954.3, 1283.7, 1168.4, and 1147.2 mAh/g, respectively. It can be found that the initial discharge capacity of the composite electrode material doped with Gd$_2$O$_3$ was significantly higher. After 100 cycles, CA@Gd$_2$O$_3$@S-2 exhibited a superior cycle stability with capacity retention of 69.7% compared to 57.3% for CA@S. The excellent cycle stability of the composite electrode material doped with Gd$_2$O$_3$ is attributed to the strong polar adsorption of polysulfide, which can better inhibit the shuttle effect of polysulfide.

The aforementioned four composite electrode materials were also subjected to high-rate charge/discharge cycles to further investigate cycle performance. As shown in Fig. 7(c), the first discharge capacities at 1 C deliver 305.2, 620.7, 763.2, and 643.6 mAh/g, respectively, and the CAs doped with Gd$_2$O$_3$ show relatively high initial discharge capacities. This is due to the catalytic effect of Gd$_2$O$_3$ on the conversion of polysulfide, which can improve the kinetic speed of electrochemical reaction and accelerate its conversion rate, thus enabling more complete discharge of sulfur. However, the ordinary CA only has a simple physical adsorption effect on the polysulfide during the discharge process and cannot catalyze its reaction, so that sulfur cannot be fully discharged when the discharge rate increases suddenly, resulting in a lower initial discharge specific capacity. CA@Gd$_2$O$_3$@S-2 still presented a high reversible specific capacity of 660.7 mAh/g with a capacity retention rate of 86.6% during 200 high-rate charge/discharge cycles at 1 C, but that of CA@S was 446.9 mAh/g, which also indicated that the CA composite electrode material doped with Gd$_2$O$_3$ still presented a preferable cycle performance at high rates.

Figure 7(d) shows the electrochemical performance of CA@S and CA@Gd$_2$O$_3$@S-n composite cathode materials at different rates. From the test results, it can be seen that the rate performance of the Gd$_2$O$_3$-doped composite electrode materials are better under a gradual increase from low to high rates. At 0.1 C, CA@Gd$_2$O$_3$@S-2 exhibited a high initial discharge capacity of 1186.3 mAh/g. When the discharge rate increased to 1 C, the discharge specific capacity of CA@Gd$_2$O$_3$@S-2 composite cathode material was 592.2 mAh/g, while the discharge specific capacity of CA@S at 0.1 C and 1 C corresponded to 916.5 and 290.7 mAh/g, respectively. The discharge specific capacity of the CA@Gd$_2$O$_3$@S-2 composite cathode material can be restored to 793.5 mAh/g at 0.2 C compared with 636.4 mAh/g for CA@S. Comparing these data with discharge specific capacities of materials prepared by other researchers (as shown in Table 1), it can be seen that the CA@Gd$_2$O$_3$@S-2 material exhibited good electrochemical properties. These results demonstrated that the CA doped with Gd$_2$O$_3$ had a good polar adsorption and catalysis effect on polysulfides. This provided the composite electrode with great redox

stability, thus improving the cycle stability of lithium-sulfur batteries at different rates. Combining the performance of the above three composites with different levels of Gd_2O_3 doping, the 0.5% Gd_2O_3-doped composite showed the best electrochemical performance.
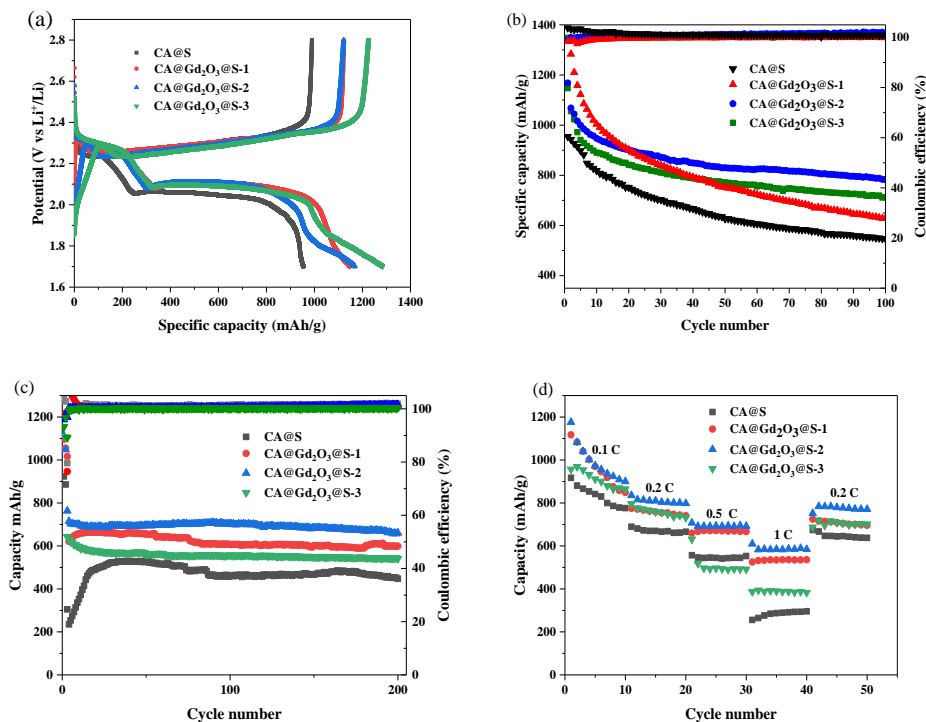

Figure 7. Electrochemical performance of the CA@S and CA@Gd_2O_3@S-n composites: (a) the initial charge/discharge curves at 0.1 C, cycling performance at (b) 0.1 C and (c) 1 C, and (d) rate capability.

Table 1. Comparison of electrochemical performance of materials prepared in other studies and the CA@Gd_2O_3@S-2 material prepared in this study

Date sources	0.2 C	1 C
CA@ N@S [18]	1338.0 mAh/g	1095.0 mAh/g
CA@ SnO_2@S [19]	780.0 mAh/g	508.0 mAh/g
CA@Gd_2O_3@S-2	793.5 mAh/g	592.2 mAh/g

To further investigate the reasons for the improved electrochemical properties, cyclic voltammetry (CV) curve tests were also performed on the synthesized materials. The CV curve of the CA@S and CA@Gd_2O_3@S-2 composite cathode materials at a scan rate of 0.1 mV/s and a voltage range of 1.7–2.8 V are shown in Figure 8. The CA@S composite cathode had two reduction peaks at 1.93 V and 2.21 V during the discharge process, corresponding to the two discharge plateaus at 1.90 V and 2.20 V in the discharge curve of this cathode material, respectively. According to the analysis of the electrochemical reaction principle of the sulfur as the cathode material, the reduction peaks appearing at 2.21 V were mainly due to the low solubility of sulfur. The reduction peak at 1.93 V was mainly due to

the further reduction of long-chain polysulfides to form short-chain polysulfides (Li_2S_2 or Li_2S), while the oxidation peak at 2.45 V was mainly due to the step-by-step oxidation of short-chain polysulfides to sulfur during the charging process [32]. The corresponding CA@Gd_2O_3@S-2 also had a similar peak structure and reaction principle, with two reduction peaks at 1.90 V and 2.22 V, and one oxidation peak at 2.45 V. In addition, the reduction and oxidation peaks of CA@Gd_2O_3@S-2 were higher than those of CA@S composite electrode material, which also shows that the addition of Gd_2O_3 enhances the conductivity of the composite material, resulting in a faster electron transfer speed and a relatively larger charge/discharge current. Moreover, the peak area of the CA@Gd_2O_3@S-2 was relatively larger, corresponding to a higher charge/discharge specific capacity. This was also due to the polar adsorption of Gd_2O_3 on polysulfide and the better catalytic effect on the redox reaction [33]. The curves of the first three cycles of the scan also coincided with each other, and no more obvious shift occurred, which demonstrates that the CA@Gd_2O_3@S-2 composite cathode material exhibited a good cycle stability.
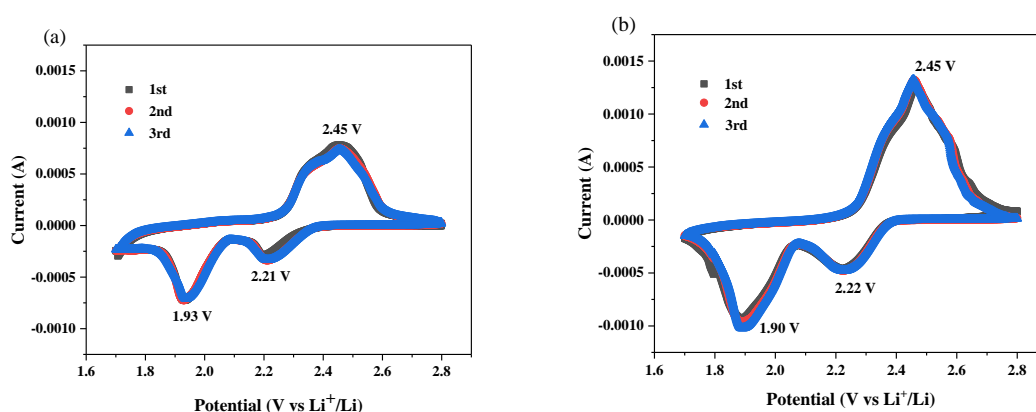

Figure 8. Cyclic voltammetry curves for the first three cycles of (a) CA@S and (b) CA@Gd_2O_3@S-2.

To analyze the lithium-ion diffusion and charge transfer during charging and discharging of CA@S and CA@Gd_2O_3@S-n composite electrodes, an AC impedance test was performed on the batteries before cycling. Figure 9 shows the AC impedance curve for the batteries composed of these four materials, which is a Nyquist plot consisting of a semicircle in the high-frequency region and a straight line in the low-frequency region. The intercept of the semicircle in the high-frequency region on the X-axis indicated ohmic impedance (R_s), while the diameter of the semicircle indicated the interfacial charge transfer resistance (R_{ct}) of the composite electrode, and the slope of the straight line in the low-frequency region indicated the Warburg diffusion impedance (W_1) of the electrode, which was mainly related to the diffusion rate of lithium ions during the cycle [34-35]. After fitting the equivalent circuit shown in Figure 9, the interfacial charge transfer resistances (R_{ct}) of CA@S and CA@Gd_2O_3@S-1, CA@Gd_2O_3@S-2, and CA@Gd_2O_3@S-3 were 192.8, 89.4, 72.6, and 86.3 Ω respectively, which indicated that the doping of Gd_2O_3 enhanced the overall conductivity of the composites and facilitated the fast electron transfer between the composites.
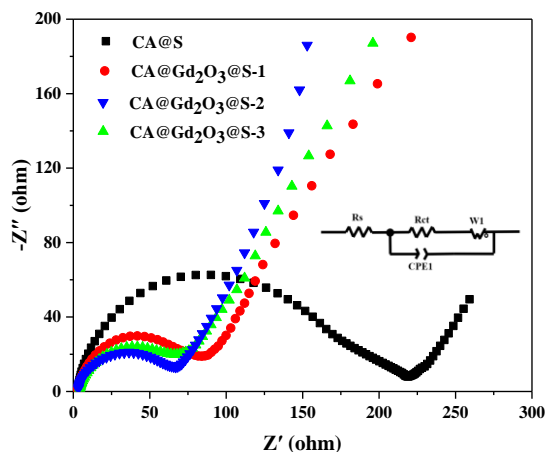
Figure 9. Equivalent circuit and Nyquist plots of CA@S and CA@Gd$_2$O$_3$@S-n.

4. CONCLUSION

In this experiment, a rare earth metal gadolinium oxide (Gd$_2$O$_3$)-doped CA composite (CA@Gd$_2$O$_3$) was prepared for loading sulfur as lithium-sulfur battery cathode materials in order to solve the problems of poor electrical conductivity and the polysulfide shuttle effect when sulfur is used as lithium-ion battery cathode material. The structure, morphology, and chemical composition of the prepared composites were verified by XRD, SEM, TEM, and XPS. The results showed that the rich pore structure of the CA alleviated the volume expansion effect of the active material sulfur. Furthermore, the physical adsorption of carbon material and the polar adsorption of Gd$_2$O$_3$ suppressed the shuttle effect of polysulfide, and the Gd$_2$O$_3$ doping also improved the overall electrical conductivity of the material. CA@Gd$_2$O$_3$@S-2 had a high sulfur-loading capacity, exhibiting a high initial specific capacity of 1168.4 mAh/g at 0.1 C and a reversible specific capacity of 814.4 mAh/g after 100 cycles. The reversible specific capacity reached 660.7 mAh/g after 200 cycles at a high rate of 1 C. The electrochemical results from several experiments showed that Gd$_2$O$_3$ had the strongest polar adsorption of polysulfides when C: Gd = 200: 1 (molar ratio). At this time, the pore structure of the CA was also maximally maintained, and the composite exhibited the best electrochemical performance.

References

1. S.H. Choi, J.H. Kim, Y.N. Ko, K.M. Yang, Y.C. Kang, *J. Power Sources*, 244 (2013) 129.
2. Z.P. Ma, G.J. Shao, X.J. Qin, Y.Q. Pan, G.L. Wang, J.J. Song, T.T. Liu, *J. Power Sources*, 269 (2014) 194.
3. X.T. Li, Z.B. Shao, K.R. Liu, Q. Zhao, G.F. Liu, B.S. Xu, *J. Solid State Electrochem.*, 23 (2019) 465.
4. P. Cui, Z.J. Jia, L.Y. Li, T. He, *J. Phys. Chem. Solids*, 72 (2011) 899.
5. P.G. Bruce, S.A. Freunberge, L.J. Hardwick, J.M. Tarascon, *Nat. Mater.*, 11 (2011) 19.
6. Q.S. Wan, P. Ping, X.J. Zhao, G.Q. Chu, J.H. Sun, C.H. Chen, *J. Power Sources*, 208 (2012) 210.
7. H. Nagata, Y. Chikusa, *J. Power Sources*, 264 (2014) 206.
8. H. Yamin, E. Peled, *J. Power Sources*, 9 (1983) 281.
9. C. Barchasz, F. Molton, C. Duboc, J.C. Lepretre, S. Patoux, *Anal. Chem.*, 84 (2012) 3973.
10. S.E. Cheon, K.S. Ko, J.H. Cho, S.W. Kim, E.Y. Chin, H.T. Kim, *J. Electrochem. Soc.*, 150 (2003) A800.
11. W.X. Su, W.J. Feng, Y. Cao, L.J. Chen, M.M. Li, C.K. Song, *Int. J. Electrochem. Sci.*, 13 (2018) 6005.
12. A.S. Ordenana-Martinez, M.E. Rincon, M. Vargas, A. Estrada-Vargas, N. Casillas, M. Barcena-Soto, E. Ramos, *J. Solid State Electrochem.*, 16 (2012) 3777.
13. M.Q. Zhao, Q. Zhang, J.Q. Huang, G.L. Tian, J.Q. Nie, H.J. Peng, F. Wei, *Nat. Commun.*, 5 (2014) 3410.
14. Y. Yuan, Z. Fang, M.B. Liu, *Int. J. Electrochem. Sci.*, 12 (2017) 1025.
15. B. Zhang, X. Qin, G.R. Li, X.P. Gao, *Energ Environ. Sci.*, 3 (2010) 1531.
16. C. Wang, K. Su, W. Wan, H. Guo, H.H. Zhou, J.T. Chen, X.X. Zhang, Y.H. Huang, *J. Mater. Chem. A*, 2 (2014) 5018.
17. M.S. Song, S.H. Han, J.H. Kim, K.T. Kim, Y.M. Kang, H.J. Ahn, S.X. Dou, J.Y. Lei, *J. Electrochem. Soc.*, 151 (2014) A791.
18. Y.Z. Shu, X.L. Li, J.J. Ye, W. Gao, S. Cheng, X.C. Zhang, L. Ma, Y.S. Ding, *Energy Technol.*, 8 (2019) 1901057.
19. M.L. Qi, X.Q. Liang, F. Wang, M.S. Han, J.H. Yin, M.H. Chen, *J. Alloy Compd.*, 799 (2019) 345.
20. M.V. Ganduglia-Pirovano, A. Hofmann, J. Sauer, *Surf. Sci. Rep.*, 62 (2007) 219.
21. X. Liang, C.Y. Kwok, F. Lodi-Marzano, Q. Pang, M. Cuisinier, H. Huang, C.J. Hart, D. Houtarde, K. Kaup, H. Sommer, *Adv. Energy Mater.*, 6 (2016) 1501636.
22. H. Sohn, M.L. Gordin, M. Regula, D.H. Kim, Y.S. Jung, J.X. Song, D.H. Wang, *J. Power Sources*, 302 (2016) 70.
23. H.C. Chen, Y.J. Wei, J.T. Wang, W.M. Qiao, L.C. Lin, D.H. Long, *ACS. Appl. Mater. Interfaces*, 7 (2015) 21188.
24. C.Y. Charles, *J. Am. Chem. Soc.*, 126 (2004) 7456.
25. Z.J. Sun, M. Xiao, S.J. Wang, D.M. Han, S.Q. Song, G.H. Chen, Y.Z. Meng, *J. Power Sources*, 285 (2015) 478.
26. H.H. Nersisyan, S.H. Joo, B.U. Yoo, D.Y. Kim, T.H. Lee, J.Y. Eom, C. Kim, K.H. Lee, J.H. Lee, *Carbon*, 103 (2016) 255.
27. X.H. Zhao, J.K. Kim, H.J. Ahn, K.K. Cho, J.H. Ahn, *Electrochim. Acta*, 109 (2013) 145.
28. H. Hu, H.Y. Cheng, Z.F. Liu, G.J. Li, Q.C. Zhu, Y. Yu, *Nano Lett.*, 15 (2015) 5116.
29. X.L. Li, L.S. Pan, Y.Y. Wang, C.S. Xu, *Electrochim. Acta*, 190 (2016) 548.
30. S. Majeed, S.A. Shivashankar, *J. Mater. Chem. B*, 2 (2014) 5585.
31. J. Liu, X.M. Tian, H.P. Chen, Y.Z. Shao, G.W. Yang, D.H. Chen, *Appl. Surf. Sci.*, 348 (2015) 60.
32. M. Cuisinier, P.E. Cabelguen, S. Evers, G. He, M. Kolbeck, A. Garsuch, T. Bolin, M. Balasubramanian, L.F. Nazar, *J. Phys. Chem. Lett.*, 4 (2013) 3227.
33. X.L. Li, Z.Q. Ding, L.Y. Zhang, R.W. Tang, Y. He, *Electrochim. Acta*, 241 (2017) 197.

34. X. Yang, L. Zhang, F. Zhang, Y. Huang, Y.S. Chen, *ACS Nano*, 8 (2014) 5208.
35. M.L. Qi, X.Q. Liang, F. Wang, M.S. Han, J.H. Yin, M.H. Chen, *J. Alloys Compd.*, 799 (2019) 345.